# Structure and magnetism of $Cr_2[BP_3O_{12}]$: Towards the quantum-classical crossover in a spin-$\frac{3}{2}$ alternating chain

O. Janson,[1,*] S. Chen,[1] A. A. Tsirlin,[1,2,†] S. Hoffmann,[1] J. Sichelschmidt,[1] Q. Huang,[3] Z.-J. Zhang,[4] M.-B. Tang,[4] J.-T. Zhao,[4] R. Kniep,[1] and H. Rosner[1,‡]

[1]*Max Planck Institute for Chemical Physics of Solids, 01187 Dresden, Germany*
[2]*National Institute of Chemical Physics and Biophysics, 12618 Tallinn, Estonia*
[3]*NIST Center for Neutron Research, Gaithersburg, Maryland 20899, USA*
[4]*Key Laboratory of Transparent Opto-Functional Inorganic Materials of Chinese Academy of Sciences, Shanghai 200050, People's Republic of China*

Magnetic properties of the spin-$\frac{3}{2}$ Heisenberg system $Cr_2[BP_3O_{12}]$ are investigated by magnetic susceptibility $\chi(T)$ measurements, electron spin resonance, neutron diffraction, and density functional theory (DFT) calculations, as well as classical and quantum Monte Carlo (MC) simulations. The broad maximum of $\chi(T)$ at 85 K and the antiferromagnetic Weiss temperature of 139 K indicate low-dimensional magnetic behavior. Below $T_N = 28$ K, $Cr_2[BP_3O_{12}]$ is antiferromagnetically ordered with the $\mathbf{k} = 0$ propagation vector and an ordered moment of $2.5\mu_B/Cr$. DFT calculations, including DFT $+ U$ and hybrid functionals, yield a microscopic model of spin chains with alternating nearest-neighbor couplings $J_1$ and $J_1'$. The chains are coupled by two nonequivalent interchain exchanges of similar strength ($\sim$1–2 K), but different sign (antiferromagnetic and ferromagnetic). The resulting spin lattice is quasi-one-dimensional and not frustrated. Quantum MC simulations show excellent agreement with the experimental data for the parameters $J_1 \simeq 50$ K and $J_1'/J_1 \simeq 0.5$. Therefore, $Cr_2[BP_3O_{12}]$ is close to the gapless critical point ($J_1'/J_1 = 0.41$) of the spin-$\frac{3}{2}$ bond-alternating Heisenberg chain. The applicability limits of the classical approximation are addressed by quantum and classical MC simulations. Implications for a wide range of low-dimensional $S = 3/2$ materials are discussed.

## I. INTRODUCTION

Magnetic properties of transition-metal compounds are generally described with the Heisenberg spin Hamiltonian that may be augmented by additional terms responsible for the anisotropy. For example, the Hamiltonian

$$H = \sum_{\langle ij \rangle} J\mathbf{S}_i \cdot \mathbf{S}_j - \sum_i D_i (\mathbf{S}_i \cdot \hat{z})^2 \qquad (1)$$

accounts for a variety of experimental situations. Here, the first term describes the isotropic coupling $J$ between spins on sites $i$ and $j$, the second term is the single-ion anisotropy $D_i$, and $\hat{z}$ is a unitary vector along $z$, whereas $\mathbf{S}_i$ and $\mathbf{S}_j$ are quantum-mechanical spin operators. Although a handful of solvable Heisenberg models exist,[1,2] the complex algebra of the spin operators generally impedes analytical solutions.

A widely used approximation of a Heisenberg model is its classical treatment: The original quantum-mechanical spin operators $\mathbf{S}_i$ are replaced by real-space vectors $\vec{S}_i$. This transformation leads to enormous alleviation of the computational effort, even if the topology of exchange couplings is very intricate.

A fundamental limitation of classical models is their inability to account for quantum-mechanical singlets and the ensuing underestimation of the ground-state (GS) energy. Indeed, for an antiferromagnetic (AF) exchange coupling $J$, the energy of the quantum-mechanical singlet state $-JS(S + 1)$ is always lower than the classical energy $-JS^2$ of the antiparallel spin arrangement. At the same time, the relative energy gain of a singlet scales as $S^{-1}$, thus being maximal for $S = 1/2$ and infinitesimal in the $S \to \infty$ limit.

Presently, there is empirical evidence that for $S \geqslant 2$ classical models capture the essential physics and correctly reproduce the experimental magnetic behavior.[3–5] In contrast, classical models often fail to predict the correct GS and magnetic excitation spectrum for the extreme "quantum" case of $S = 1/2$.[6,7] Further on, many $S = 1$ systems, e.g., one-dimensional (1D) Haldane chains,[8] cannot be treated classically. Therefore, it is crucial to establish the applicability limits for the classical approximation in order to distinguish between the "classical" cases amenable to a simplified model treatment and the "quantum" cases that require the complete quantum-mechanical solution of the spin Hamiltonian.

A feasible way towards better understanding of these limits are real material studies that allow for a direct comparison between theory and experiment. Previous work on the quantum-classical crossover rendered the quasi-1D $S = 3/2$ magnets as the relevant playground. Despite the relatively large spin of 3/2, the pronounced one-dimensionality may lead to sizable quantum fluctuations and, thus, to deviations from the classical behavior. For example, inelastic neutron scattering (INS) studies of $Cs[VX_3]$ ($X =$ Cl, Br) evidence that at high temperatures these materials are classical, while lowering the temperature results in a crossover to the quantum behavior.[9] The INS experiments on the quasi-1D magnet $AgCr[P_2S_6]$ yielded a sizable discrepancy between the observed spin-wave velocity and its classical value, thus indicating strong quantum effects that are present in $S = 3/2$ chains.[10]

Here, we present a joint experimental and theoretical study of the quasi-1D $S = 3/2$ system $Cr_2[BP_3O_{12}]$. Its crystal structure features magnetic $Cr(III)_2O_9$ blocks embedded into a complex borophosphate framework (Fig. 1). Although this

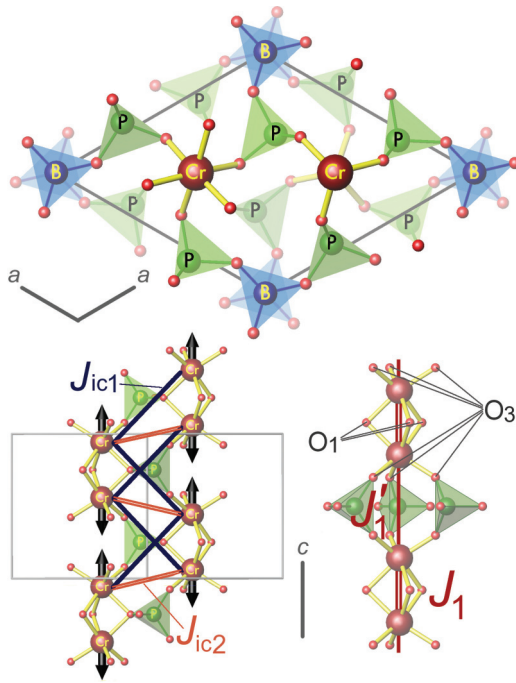FIG. 1. (Color online) Crystal structure of $Cr_2[BP_3O_{12}]$. (Top) View along [0001]. (Bottom left) View perpendicular to [0001]. The pathways of the leading interchain couplings $J_{ic1}$ and $J_{ic2}$ are shown with dark gray (dark blue) and light gray (red) lines, respectively. Thick arrows denote the experimental magnetic structure refined in $\Gamma_1$ (see Sec. III B for details). (Bottom right) Dimers are connected via three $PO_4$ tetrahedra and form chains running along [0001]. The intradimer coupling $J_1$ (double line) as well as the interdimer coupling $J_1'$ (single line) are shown.

type of crystal structure could lead to the simple magnetism of isolated spin dimers, neutron diffraction and magnetic susceptibility measurements evidence long-range AF ordering at $T_N = 28$ K that is indicative of sizable interdimer couplings. Using extensive density functional theory (DFT) calculations, we evaluate a microscopic magnetic model for this compound and establish the spin lattice of weakly coupled bond-alternating Heisenberg chains. This theoretical model is in good agreement with the neutron scattering and magnetic susceptibility data.

As the microscopic magnetic model of $Cr_2[BP_3O_{12}]$ lacks frustration, its properties can be simulated with the computationally efficient quantum Monte Carlo (QMC) techniques. At the same time, the classical model on the same spin lattice can be treated using classical Monte Carlo (MC) algorithms. By comparing the QMC and classical MC results, we evaluate the relative impact of quantum as well as thermal fluctuations on the spin correlations, and in this way address the crossover between the quantum and classical behaviors.

This paper is organized as follows. The experimental as well as numerical methods are described in Sec. II. The experimental part in Sec. III comprises the results of neutron diffraction, electron spin resonance (ESR), and magnetic susceptibility measurements. The DFT-based evaluation of the microscopic magnetic model (Sec. IV) is followed by the refinement of model parameters by means of QMC simulations and subsequent fitting to the experiment (Sec. V).

The differences between the quantum model and its classical counterpart are discussed in Sec. VI. We summarize our results and give a short outlook in Sec. VII.

## II. METHODS

$Cr_2[BP_3O_{12}]$ was prepared by the Pechini-type method.[11] Chromium acetate (2.172 g) [Alfa Aesar, 23.37(5) wt% chromium content] and 5.7945 g citric acid (Alfa Aesar 99 + %) were dissolved in 50 ml water. Glycerol (5 ml) (Sigma 99%) and a well-ground mixture of 0.3197 g boric acid (Sigma) and 1.7613 g ammonium dihydrogen phosphate (Merck) were added to the dark green solution. After slow evaporation of water, a transparent resin was formed which was dried at 200 °C for 2 h. The obtained product was crushed and transferred to a corundum crucible. The first heating at 850 °C for 12 h yielded a gray-green product. Several annealing steps with grinding in between followed. The final product was obtained after heat treatment at 1000 °C for 48 h.

The powder x-ray diffraction pattern (Huber image plate Guinier camera G670, Ge monochromator, Cu $K_{\alpha1}$ radiation, $\lambda = 1.5406$ Å, powdered sample fixed with Vaseline between two Mylar foils, each 6 $\mu$m thick) indicated the formation of single-phase $Cr_2[BP_3O_{12}]$.[12]

Neutron powder diffraction data were collected[13] using the BT-1 high-resolution powder diffractometer at the NIST Center for Neutron Research. A monochromatic neutron beam with the wavelength of 1.5403 Å was produced by a Cu (311) monochromator. Collimators with horizontal divergences of 15′, 20′, and 7′ full width at half maximum were used before and after the monochromator and after the sample, respectively. The intensities were measured in steps of 0.05° in the $2\theta$ range 3°–168°. The data were collected at 4 K, 35 K, and 300 K. Additionally, the magnetic scattering was studied with the triple-axis spectrometer BT-7 using the wavelength of 2.359 Å. The intensity of the strongest magnetic reflection was monitored with the step of 0.5 K in the 5 K–35 K temperature range. The structural analysis was performed using the program GSAS.[14] The magnetic structure was refined with FULLPROF.[15]

The magnetic susceptibility was measured using a commercial Quantum Design MPMS SQUID in the temperature range 2 K–380 K in magnetic fields up to 5 T. The ESR measurement was performed at room temperature with a standard continuous-wave spectrometer at $X$-band frequencies ($\nu \approx 9.5$ GHz) by using a cylindrical resonator in $TE_{012}$ mode.

DFT calculations have been performed using the full-potential local-orbital code FPLO9.00-33 (Ref. 16) and the pseudopotential projector-augmented-wave code VASP-5.2 (Ref. 17). For the scalar-relativistic calculations, we used the local density approximation (LDA)[18] and generalized gradient approximation (GGA)[19] exchange-correlation potentials. Spin-unpolarized calculations were performed on a $14 \times 14 \times 14$ mesh of $k$ points. For the spin-polarized calculations (DFT, DFT + $U$), we doubled the cell along $c$ and used a $4 \times 4 \times 2$ $k$ mesh. Hybrid-functional calculations were performed in VASP using the HSE06 functional[20] on a $2 \times 2 \times 2$ $k$ mesh.[21] The convergence with respect to the $k$ meshes has been accurately checked. All calculations have

TABLE I. Crystallographic data for Cr$_2$[BP$_3$O$_{12}$] (space group $P6_3/m$) according to the neutron powder diffraction data at 4, 35, and 300 K.

| $T$ | | 4 K | | | 35 K | | | 300 K | | |
|---|---|---|---|---|---|---|---|---|---|---|
| $a$ (Å) | | 7.9444(2) | | | 7.9448(2) | | | 7.9524(2) | | |
| $c$ (Å) | | 7.3439(3) | | | 7.3448(3) | | | 7.3543(3) | | |
| $V$ (Å$^3$) | | 401.40(2) | | | 401.49(3) | | | 402.78(3) | | |
| $R_\mathrm{p}$ (%) | | 5.5 | | | 5.8 | | | 6.4 | | |
| $R_\mathrm{wp}$ (%) | | 6.9 | | | 7.6 | | | 7.9 | | |
| $R_\mathrm{exp}$ (%) | | 6.1 | | | 7.5 | | | 8.4 | | |
| | | $x/a$ | $y/b$ | $z/c$ | $x/a$ | $y/b$ | $z/c$ | $x/a$ | $y/b$ | $z/c$ |
| Cr | $4f$ | 1/3 | 2/3 | 0.0578(8) | 1/3 | 2/3 | 0.0614(9) | 1/3 | 2/3 | 0.0590(7) |
| P | $6h$ | 0.3657(4) | 0.3166(5) | 1/4 | 0.3658(4) | 0.3168(5) | 1/4 | 0.3653(4) | 0.3159(5) | 1/4 |
| B | $2a$ | 0 | 0 | 1/4 | 0 | 0 | 1/4 | 0 | 0 | 1/4 |
| O1 | $6h$ | 0.4023(4) | 0.5254(4) | 1/4 | 0.4009(4) | 0.5249(5) | 1/4 | 0.3997(4) | 0.5255(5) | 1/4 |
| O2 | $6h$ | 0.1362(4) | 0.1931(4) | 1/4 | 0.1351(5) | 0.1924(4) | 1/4 | 0.1358(4) | 0.1926(4) | 1/4 |
| O3 | $12i$ | 0.4368(3) | 0.2691(3) | 0.0774(2) | 0.4365(3) | 0.2697(4) | 0.0768(3) | 0.4382(3) | 0.2716(3) | 0.0786(3) |

been performed based on the crystal structure determined at 4 K, as given in Table I.

QMC simulations were performed using the code LOOPER from the software package ALPS version 1.3.[22] The magnetic susceptibility was simulated on $8 \times 8 \times 64$ finite lattices of $S = 3/2$ spins in the temperature range $0.25J_1–8J_1$, corresponding to 12.5 K–400 K (see Sec. V) using 30 000 sweeps for thermalization and 300 000 sweeps after thermalization. The statistical errors ($<0.5\%$) are below the experimental accuracy. For simulations of the spin stiffness and the static structure factor, we used finite lattices up to 13 824 and 2048 spins, respectively.

For the classical MC simulations, we used the SPINMC code,[22] with 200 000 and 2 000 000 sweeps for and after thermalization, respectively. The length of the classical vectors is chosen such that the maximal diagonal correlation matches the exact quantum result. Chains of $N = 800$ spins were evaluated. Exact diagonalization of the $S^z = 0$ sector was performed for $N = 14$ sites alternating $S = 3/2$ chain using SPARSEDIAG from the ALPS package.[22]

## III. EXPERIMENTAL RESULTS

### A. Crystal structure

The crystal structure of Cr$_2$[BP$_3$O$_{12}$] has been initially refined from x-ray powder data in the space group $P3$.[12] However, the crystal structures of related $M$(III)$_2$[BP$_3$O$_{12}$] borophosphates were determined ($M =$ In) or redetermined ($M =$ Fe) from single-crystal data in the space group $P6_3/m$.[23] This apparent mismatch led us to reconsider the crystal structure of Cr$_2$[BP$_3$O$_{12}$]. A thorough analysis of both x-ray and neutron powder patterns identified the reflection condition $00l$ with $l = 2n$, which is characteristic of the $6_3$ screw axis. No other reflection conditions could be observed, so that the list of possible space groups is restricted to $P6_3$, $P6_3/m$, and $P6_322$. While the refinement in $P6_322$ was unsuccessful, the space group $P6_3/m$ resulted in low residuals and a fully ordered crystal structure. Therefore, this centrosymmetric space group was preferred over its noncentrosymmetric subgroup $P6_3$. No significant structural changes between 4 K and room temperature were detected.

Crystallographic data are listed in Table I. Selected interatomic distances at 4 K are given in Table II.

The structure solution of Cr$_2$[BP$_3$O$_{12}$] in the space group $P6_3/m$ is consistent with earlier results for other $M_2$[BP$_3$O$_{12}$] transition-metal borophosphates.[23] Their crystal structures are isotypic and feature dimers of face-sharing $M$O$_6$ octahedra (Fig. 1, bottom). The octahedra exhibit a sizable trigonal distortion leading to two groups of nonequivalent Cr-O distances. The shorter Cr-O3 distances of about 1.91 Å (at 4 K) take the terminal position of the Cr$_2$O$_9$ dimer, whereas the longer Cr-O1 distances of about 2.04 Å are bridging (Fig. 1, bottom right). The formation of longer Cr-O distances in the bridging position is due to the Cr-Cr contact remaining relatively long (about 2.8 Å), in order to reduce the repulsion between the positively charged Cr$^{3+}$ ions. PO$_4$ tetrahedra link the Cr$_2$O$_9$ dimers along [0001], whereas the BO$_3$ triangles interconnect the PO$_4$ tetrahedra and do not share oxygen atoms with the CrO$_6$ octahedra (Fig. 1, top).

### B. Magnetic structure

At 4 K, an additional magnetic scattering was observed. The only visible magnetic reflection is at $2\theta \simeq 17.6°$ and matches the weak 101 reflection of the nuclear structure. As the Néel temperature of Cr$_2$[BP$_3$O$_{12}$] is $T_N \simeq 28$ K (see below) and no structural changes below $T_N$ are expected, the subtraction of the 35 K data from the 4 K data results in the purely magnetic scattering (Fig. 2, inset). However, no clear signatures of other magnetic reflections could be observed.

According to BASIREPS, the $P6_3/m$ space group, the $\mathbf{k} = 0$ propagation vector, and the $4f$ Wyckoff position of Cr allow for 12 irreducible representations with the magnetic moments lying in the $ab$ plane or pointing along the $c$ direction. Most of these representations can be discarded because they produce

TABLE II. Selected interatomic distances (in Å) in the Cr$_2$[BP$_3$O$_{12}$] crystal structure at 4 K.

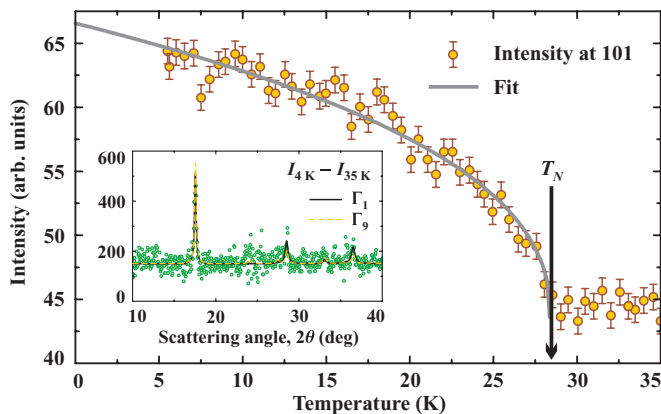| Cr$-$O1 | $3 \times 2.041(5)$ | P$-$O1 | 1.535(4) |
|---|---|---|---|
| Cr$-$O3 | $3 \times 1.910(3)$ | P$-$O2 | 1.580(4) |
| Cr$-$Cr | 2.823(11) | P$-$O3 | $2 \times 1.511(2)$ |
| B$-$O2 | $3 \times 1.365(3)$ | | |

FIG. 2. (Color online) Cr$_2$[BP$_3$O$_{12}$]. Temperature evolution of the magnetic 101 reflection (circles) and the fit with Eq. (2). The residual intensity above $T_N$ is due to the nuclear scattering and background. (Inset) Refinement of the subtracted ($I_{4\,K} - I_{35\,K}$) pattern with spins along $c$ ($\Gamma_1$, dark solid line) and along $a$ ($\Gamma_9$, light dashed line). Note that the temperature scan (main figure) and the angular scan (inset) are done on different instruments; hence, the respective intensities should not be compared.

the largest magnetic reflection at 100, 110, or 111, which is contrary to the experimental observation of the magnetic scattering at 101 (Fig. 2, inset). The refinement is possible only in two representations, $\Gamma_1$ and $\Gamma_9$, that entail the same ordering pattern (Fig. 1, bottom left) with the magnetic moments along $c$ and $a$, respectively.

To evaluate the ordered magnetic moment, we refined the subtracted pattern as the purely magnetic phase, and fixed the scale factor according to the refinement of the 35 K pattern, which is free from magnetic scattering. The resulting magnetic moment at 4 K is 2.5(1)$\mu_B$ in $\Gamma_1$ and 1.1(1)$\mu_B$ in $\Gamma_9$, with the refinement residuals of 0.131 in both models. While the refinements within $\Gamma_1$ and $\Gamma_9$ are slightly different at high angles (see the inset of Fig. 2), the quality of the powder data is insufficient to observe these marginal differences and to discriminate between the two models. However, the spin-only magnetic moment of 3$\mu_B$, which is expected for the $S = 3/2$ Cr$^{3+}$ ion, strongly favors the solution in $\Gamma_1$. The somewhat lower experimental value of 2.5$\mu_B$ is due to quantum fluctuations (see Sec. V).

The magnetic structure of Cr$_2$[BP$_3$O$_{12}$] is shown in Fig. 1 (bottom left). We find that the Cr moments are antiferromagnetically ordered within each Cr$_2$O$_9$ dimer. The interdimer ordering is also AF, both in the $ab$ plane and along the $c$ direction.

Temperature evolution of the magnetic moment can be tracked by the temperature dependence of the magnetic reflection 101 (Fig. 2). These data are fitted with the empirical formula

$$I(T) = I_{bg} + I_0 \left( 1 - \frac{T}{T_N} \right)^\beta, \qquad (2)$$

where $I_{bg}$ refers to the nuclear scattering and background above $T_N$. The fit yields the Néel temperature $T_N = 28.2(7)$ K and the critical exponent $\beta = 0.38(3)$. The estimated $T_N \simeq 28$ K is in excellent agreement with the magnetic susceptibility measurement presented below (Fig. 3), whereas $\beta$ falls into the
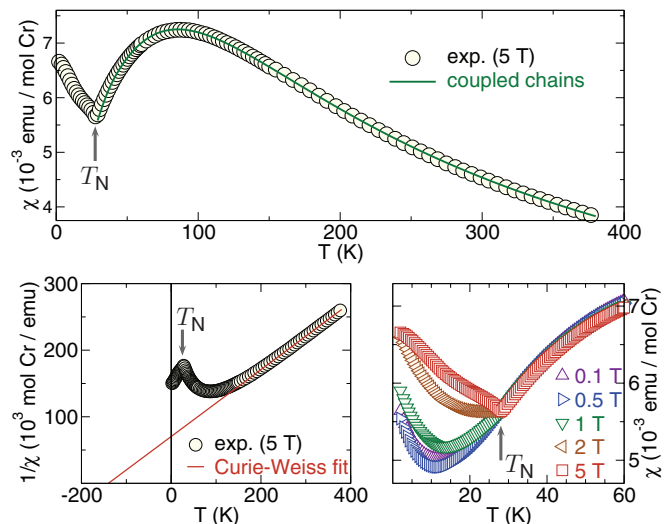


FIG. 3. (Color online) (Top) Experimental magnetic susceptibility $\chi(T)$ of Cr$_2$[BP$_3$O$_{12}$] measured at 5 T (circles) and fit with the model of coupled bond-alternating $S = 3/2$ chains (line). (Bottom left) Curie-Weiss fit to experimental $\chi(T)$. (Bottom right) Field dependence of $\chi(T)$. Note the long-range AF ordering transition at $T_N = 28$ K.

range of values (0.36–0.39) proposed for the 3D Heisenberg model.[24]

### C. Magnetic susceptibility and ESR

The temperature dependence of the magnetic susceptibility $\chi(T)$ (Fig. 3, top) reveals a typical low-dimensional behavior with a broad maximum around $T = 85$ K. The high-temperature part ($T > 200$ K) of the curve obeys the Curie-Weiss law (Fig. 3, bottom left) with the Curie constant $C = 1.987$ emu K (mol Cr)$^{-1}$ leading to the effective magnetic moment $\mu_{eff} = \sqrt{3Ck_B\mu_B^{-2}N_A^{-1}} = 3.987\mu_B$ per Cr, which is slightly larger than the spin-only contribution $\mu_{eff} = g\sqrt{S(S+1)} \simeq 3.88\mu_B$ (assuming the orbital moment is completely quenched).

The Weiss temperature $\theta = 139$ K and the broad maximum around $T^{max} = 85$ K, corresponding to $\sim$61% of $\theta$, indicate sizable AF spin correlations. The magnetic ordering temperature $T_N = 28$ K can be clearly traced by the divergence of the $\chi(T)$ curves measured in low and high fields. While the low-field measurements show only an inconspicuous bend around $T_N$, the measurements above 2 T reveal a well-defined cusp. This divergence is due to the spin-flop transition in the AF-ordered phase. The spin-flop transition indeed takes place at about 1.7 T, as shown by the low-temperature magnetization curve.[25]

Room-temperature ESR measurements yield a narrow line that can be fitted with a single powder-averaged Lorentzian.[25] Within resolution, the resonance field appears isotropic and corresponds to the $g$ value of 1.968, which indicates weak spin-orbit coupling, as typical for Cr$^{3+}$.

The low-dimensional magnetism of Cr$_2$[BP$_3$O$_{12}$] is consistent with the presence of Cr$_2$O$_9$ dimers in the crystal structure. However, isolated spin dimers should have a singlet GS at low temperatures. The fact that Cr$_2$[BP$_3$O$_{12}$] develops long-range AF order with a sizable Néel temperature of 28 K

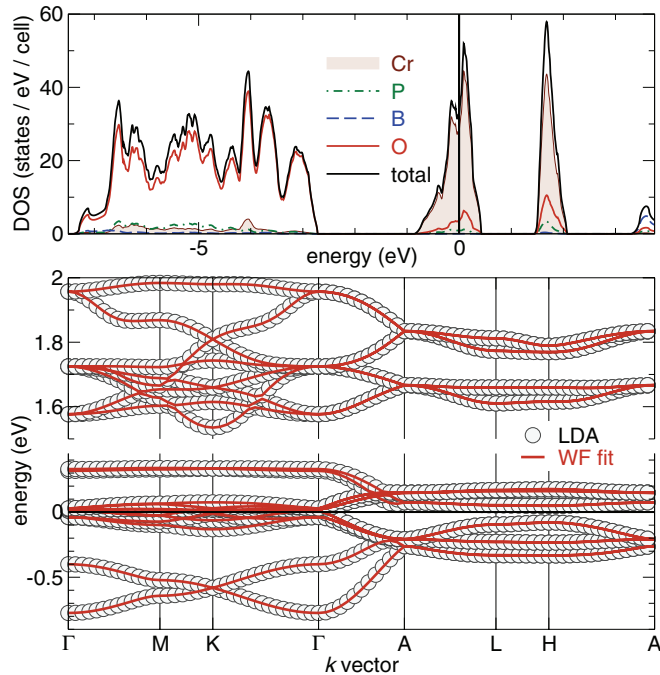FIG. 4. (Color online) Electronic structure of $Cr_2[BP_3O_{12}]$. (Top) LDA density of states. The Fermi level $\varepsilon_F$ is at zero energy. The contribution from Cr states is shown by shaded filling. (Bottom) LDA bands in the vicinity of the Fermi level and the fit with the tight-binding model based on Wannier functions.

implies substantial interdimer couplings via the $PO_4$ groups. While such couplings are abundant in vanadium and copper phosphates,[26–28] their identification is by no means a simple task. For example, in $Cr_2[BP_3O_{12}]$ the shortest interdimer Cr-Cr distances are 4.55 Å along [0001] and 4.67 Å in the (0001) plane, and it is impossible to decide *a priori* whether one of these pathways is more efficient, or both should be treated on equal footing. To develop a reliable magnetic model of $Cr_2[BP_3O_{12}]$, we perform extensive DFT calculations followed by QMC simulations, and provide detailed microscopic insight into the magnetism of this compound.

## IV. DFT CALCULATIONS

To unravel the microscopic origin of the observed low-dimensional magnetic behavior, we apply DFT calculations and evaluate the individual exchange couplings. Nonmagnetic (spin-unpolarized) calculations within both LDA and GGA yield a well-structured valence band (Fig. 4, top) with the total width of ~10 eV, crossed by the Fermi level $\varepsilon_F$ at zero energy. This metallic electronic GS, contrasting with the green color of $Cr_2[BP_3O_{12}]$, originates from the underestimation of the strong electron-electron repulsion within the Cr $3d$ shell. Technically, the band gap can be readily restored in a spin-polarized calculation, due to the sizable exchange splitting typical for $Cr^{3+}$. However, its value is too small (1.29 eV in LSDA, 1.78 eV in GGA)[25] to account for the green color ($\simeq$2.2–2.5 eV) of $Cr_2[BP_3O_{12}]$. Accounting for electronic correlations is challenging, since many-body effects cannot be properly described within the one-electron approach of conventional DFT functionals.

Typically, multiorbital correlated insulators are described by an extended Hubbard model that comprises the kinetic terms (electron transfer), the on-site and intersite correlations (Coulomb repulsion), and the on-site exchange (Hund's exchange). However, the large Hilbert space of such models impedes even an approximate numerical solution that would establish a simple relation between the parameters of the Hubbard model and the resulting magnetic couplings. Therefore, we restrict ourselves to a qualitative analysis of electron transfers.

For the quantitative evaluation of magnetic couplings, we account for correlation effects using the mean-field-like DFT + U approach or the hybrid (DFT + exact exchange) functionals. The comparison to the experiment demonstrates the good agreement between different computational approaches and underscores the validity of the qualitative analysis based on the electron transfers. Thus, this qualitative model approach could also be used as a starting point for more involved $Cr^{3+}$ systems with nontrivial coupling pathways.

### A. Qualitative model approach

Conventional DFT (LDA and GGA) functionals are known for their accurate description of electron transfer processes; thus, kinetic terms of the model Hamiltonian can be evaluated directly from the LDA/GGA band dispersions for the Cr $3d$ states. Typical for an octahedral environment, these states split into two manifolds: half-filled $t_{2g}$ orbitals centered at $\varepsilon_F$ and empty $e_g$ orbitals that lie ~1.7 eV higher in energy owing to the sizable crystal-field splitting.

Altogether, the $t_{2g}$ and $e_g$ manifolds comprise 20 bands, in line with five $3d$ orbitals per Cr atom and four Cr atoms in a unit cell. To evaluate the transfer integrals $t_{ij}^{mm'}$ ($m$ and $m'$ are orbital indices, $i$ and $j$ are site indices), we map these 20 bands onto an effective five-orbital tight-binding model, and parametrize this model using the Wannier functions (WFs) technique.[29] In the WF basis (Fig. 5), the couplings $t_{ij}^{mm'}$ are evaluated as nondiagonal matrix elements. The resulting $t_{ij}^{mm'}$ show excellent agreement between the tight-binding model and the computed LDA/GGA band dispersions (Fig. 4, bottom).

Sizable transfer integrals are found for four Cr-Cr pathways (Table III): The intradimer transfer ($t_1$), the interdimer tranfer along $c$ ($t_1'$), the shortest interdimer pathway in the $ab$ plane ($t_{ic2}$), and the longer interdimer pathway along the [2$\bar{2}$3] direction ($t_{ic1}$); see Fig. 1. Here, $t_1'$ and $t_{ic2}$ run via triple bridges of the $PO_4$ polyhedra (along $c$), whereas $t_{ic1}$ runs via a single $PO_4$ tetrahedron. Other couplings are negligible, as they involve the transfer through at least two $PO_4$ tetrahedra in a row.

Although an explicit expression relating exchange integrals $J_{ij}$ to transfer integrals $t_{ij}^{mm'}$ is presently not available, the qualitative comparison of $t_{ij}^{mm'}$ terms elucidates different contributions to the magnetic exchange. According to the Goodenough-Kanamori rules, the hoppings between the half-filled states (both $m$ and $m'$ belong to the $t_{2g}$ subspace) are responsible for AF couplings, whereas the hoppings between the half-filled and empty states ($m$ belongs to $t_{2g}$, $m'$ belong to $e_g$) give rise to ferromagnetic (FM) interactions.
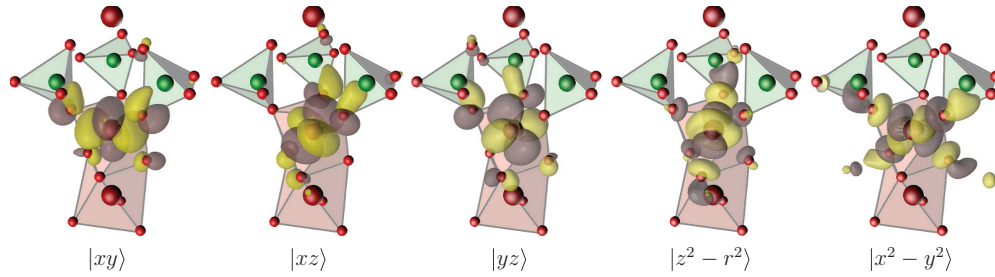
FIG. 5. (Color online) $Cr_2[BP_3O_{12}]$: Wannier functions for five Cr $3d$ orbitals (see subscripts). Cr, P, and O atoms are depicted by large (red), intermediate-size (green), and small (red) spheres, respectively. For each of the five WFs, a $Cr_2O_9$ dimer and three $PO_4$ tetrahedra are shown. The projection is similar to the bottom right panel of Fig. 1.

First, we consider the intradimer $t_1^{mm'}$ hoppings, where the couplings between different $t_{2g}$ orbitals are dominant: $t_1^{xy,xz} = t_1^{xz,yz} = t_1^{yz,xy} = -125$ meV. At the same time, the largest hopping between the $t_{2g}$ and $e_g$ orbitals is smaller ($t_1^{xy,z^2-r^2} = -97$ meV), thus hinting at the AF nature of $J_1$. For the interdimer coupling $t_1'$ the difference is even more

TABLE III. Leading transfer integrals $t_i^{mm'}$ (notation according to Fig. 1), where $m$ and $m'$ are orbital indices from the following set: $|xy\rangle$, $|xz\rangle$, $|yz\rangle$, $|z^2-r^2\rangle$, and $|x^2-y^2\rangle$. All values are given in meV. For clarity, only one of two symmetrically equivalent terms $t_{ij}^{mm'}$ and $t_{ij}^{m'm}$ is shown. The Cr-Cr distances ($d_{\text{Cr-Cr}}$) are given for the 4 K structure (Table I).

| | $t_1$ ($d_{\text{Cr-Cr}} = 2.823$ Å) | | | | |
| | $\|xy\rangle$ | $\|xz\rangle$ | $\|yz\rangle$ | $\|z^2-r^2\rangle$ | $\|x^2-y^2\rangle$ |
|---|---|---|---|---|---|
| $\langle xy\|$ | $-38$ | $-125$ | $-125$ | $-97$ | |
| $\langle xz\|$ | | $-38$ | $-125$ | $39$ | $-89$ |
| $\langle yz\|$ | | | $-38$ | $58$ | $78.9$ |
| $\langle z^2-r^2\|$ | | | | | |
| $\langle x^2-y^2\|$ | | | | | |

| | $t_1'$ ($d_{\text{Cr-Cr}} = 4.521$ Å) | | | | |
| | $\|xy\rangle$ | $\|xz\rangle$ | $\|yz\rangle$ | $\|z^2-r^2\rangle$ | $\|x^2-y^2\rangle$ |
|---|---|---|---|---|---|
| $\langle xy\|$ | $-124$ | | | | |
| $\langle xz\|$ | | $-124$ | | $33$ | |
| $\langle yz\|$ | | | $-124$ | | |
| $\langle z^2-r^2\|$ | | | | $-60$ | |
| $\langle x^2-y^2\|$ | | | | | $-60$ |

| | $t_{\text{ic1}}$ ($d_{\text{Cr-Cr}} = 5.875$ Å) | | | | |
| | $\|xy\rangle$ | $\|xz\rangle$ | $\|yz\rangle$ | $\|z^2-r^2\rangle$ | $\|x^2-y^2\rangle$ |
|---|---|---|---|---|---|
| $\langle xy\|$ | | | | $86$ | $-60$ |
| $\langle xz\|$ | | | | $-44$ | $75$ |
| $\langle yz\|$ | | | | $-67$ | |
| $\langle z^2-r^2\|$ | | | | $30$ | $35$ |
| $\langle x^2-y^2\|$ | | | | | $38$ |

| | $t_{\text{ic2}}$ ($d_{\text{Cr-Cr}} = 4.665$ Å) | | | | |
| | $\|xy\rangle$ | $\|xz\rangle$ | $\|yz\rangle$ | $\|z^2-r^2\rangle$ | $\|x^2-y^2\rangle$ |
|---|---|---|---|---|---|
| $\langle xy\|$ | | $-30$ | $-30$ | | |
| $\langle xz\|$ | | | | | |
| $\langle yz\|$ | | | | | |
| $\langle z^2-r^2\|$ | | | | | |
| $\langle x^2-y^2\|$ | | | | | $-31$ |

pronounced: The hoppings between $t_{2g}$ orbitals amount to $-124$ meV, thus dominating over the hopping to the empty $z^2-r^2$ orbital. Therefore, the interdimer exchange $J_1'$ should be also AF.

The interchain coupling $J_{\text{ic2}}$ is realized primarily via $t_{\text{ic2}}^{xy,xz}$ and $t_{\text{ic2}}^{xy,yz}$ hoppings; hence, the AF contribution is again dominant. In contrast, for the interchain coupling $J_{\text{ic1}}$, the $t_{2g} \rightarrow t_{2g}$ hoppings are close to zero, whereas the $t_{2g} \rightarrow e_g$ hoppings are still sizable. Therefore, the overall exchange should be FM.

The above qualitative analysis is confirmed by elaborate DFT + $U$ and hybrid-functional calculations reported below. More importantly, the proposed couplings are in agreement with the experimental magnetic structure that features antiparallel spins along $J_1$, $J_1'$, and $J_{\text{ic2}}$ (Fig. 1, bottom left panel). The respective AFM couplings establish parallel spins along the $J_{\text{ic1}}$ bonds that are indeed FM. Therefore, the spin lattice of $Cr_2[BP_3O_{12}]$ is nonfrustrated. Because $J_1' \gg J_{\text{ic1}}, J_{\text{ic2}}$, this spin lattice can be considered as quasi-1D, with bond-alternating $J_1 - J_1'$ chains running along the $c$ direction.

### B. Total-energy calculations

A sizable exchange splitting typical for $Cr^{3+}$ compounds readily opens a band gap (albeit underestimating the experimental value; see Ref. 25) in the spin-polarized calculations, so that the magnetic energy can be evaluated directly from LSDA or GGA total-energy calculations. In particular, total energies $E_{\text{tot}}$ corresponding to different collinear magnetic configurations can be mapped onto classical Heisenberg model, thus yielding the exchange integrals $J_{ij}$:

$$E_{\text{tot}} = E_0 + E_{\text{magn}} = E_0 + \sum_{\langle i,j\rangle} J_{ij} \vec{S}_i \cdot \vec{S}_j. \qquad (3)$$

We apply this approach to evaluate the intrachain and interchain couplings. In LSDA, we obtain $J_1 = 151$ K and $J_1' = 82$ K, as well as the FM $J_{\text{ic1}} = -8$ K and the AF $J_{\text{ic2}} = 2$ K. Spin-polarized GGA yields marginally smaller values (Table IV). To challenge these estimates, we address the Weiss temperature $\theta$, which is a linear combination of magnetic couplings.[30] For the $Cr_2[BP_3O_{12}]$ spin lattice, the expected Weiss temperature is

$$\theta = \tfrac{1}{3}S(S+1)(J_1 + J_1' + 6J_{\text{ic1}} + 3J_{\text{ic2}}), \qquad (4)$$

where each coupling is summed up according to its coordination number in the spin lattice. Adopting the values

TABLE IV. Leading exchange integrals $J_i$ (in K) calculated with different DFT-based methods. For the DFT $+\,U$ results, the double-counting correction (DCC) and $U_d$ value (in eV) are given. For the HSE06 hybrid functional, the admixture of the exact exchange ($\beta$) is specified.

| $E_{\mathrm{xc}}$ (DCC) | $U_d$ or $\beta$ | $J_1$ | $J_1'$ | $J_{\mathrm{ic2}}$ | $J_{\mathrm{ic1}}$ | $J_1'/J_1$ |
|---|---|---|---|---|---|---|
| LSDA | | 150 | 82 | 2.5 | −7.8 | 0.55 |
| GGA | | 125 | 63 | 2.2 | −5.6 | 0.51 |
| | 2.0 | 109 | 60 | 2.3 | 0.1 | 0.62 |
| LSDA $+\,U$ (AMF) | 3.0 | 89 | 55 | 2.2 | 1.7 | 0.72 |
| | 4.0 | 70 | 50 | 2.1 | 2.8 | 0.86 |
| | 2.0 | 84 | 49 | 1.6 | −2.1 | 0.58 |
| LSDA $+\,U$ (FLL) | 3.0 | 54 | 38 | 1.2 | −1.8 | 0.71 |
| | 4.0 | 33 | 31 | 0.9 | −1.6 | 0.94 |
| | 2.0 | 97 | 48 | 2.2 | 1.0 | 0.50 |
| GGA $+\,U$ (AMF) | 3.0 | 81 | 44 | 2.1 | 2.3 | 0.54 |
| | 4.0 | 67 | 41 | 2.1 | 3.3 | 0.61 |
| | 2.0 | 78 | 40 | 1.6 | −1.0 | 0.51 |
| GGA $+\,U$ (FLL) | 3.0 | 54 | 32 | 1.2 | −1.0 | 0.59 |
| | 4.0 | 37 | 26 | 1.0 | −0.9 | 0.69 |
| | 0.20 | 66 | 27 | 1.2 | −2.5 | 0.41 |
| HSE06 | 0.25 | 58 | 23 | 1.0 | −2.0 | 0.40 |
| | 0.30 | 51 | 20 | 0.9 | −1.7 | 0.39 |

of $J_i$ from LSDA (GGA), we obtain $\theta \simeq 242$ K (202 K), which is 50%–70% larger than the experimental value $\theta = 139$ K.

This discrepancy primarily originates from the poor description of electronic correlations within LDA or GGA, and calls for the application of more elaborate computational approaches. For strongly correlated insulators, such as Cr$_2$[BP$_3$O$_{12}$], the mean-field DFT $+\,U$ method is a natural choice. An intrinsic problem of this method is the double counting (DC) of the correlation energy already present in LDA or GGA. This correlation energy should be subtracted from the total energy of the system. In the widely used DC corrections, denoted around-mean-field (AMF) and fully localized limit (FLL),[31] the subtracted energy corresponds to the energy of the uniformly occupied state or the state with integer occupation numbers, respectively. Previous DFT $+\,U$ studies on Cr$^{3+}$ materials[32] did not render any of the two schemes preferable; thus, we apply both and compare their results with the experiment.

Besides the DC, the DFT $+\,U$ method introduces two free parameters: the on-site repulsion $U_d$ and the on-site exchange $J_d$. While an empirical evidence favors $J_d \simeq 1$ eV for $3d$ elements, the values of $U_d$ can substantially vary depending on the electronic configuration and local environment of the magnetic ion. For Cr$^{3+}$, we varied $U_d$ in the range between 2 and 4 eV.[32,33]

The resulting DFT $+\,U$-based exchange integrals are listed in Table IV. We find that the exchange integrals are weakly dependent on the DFT exchange-correlation potential (LSDA or GGA). In contrast, the DC correction plays a more substantial role: The calculations within AMF yield considerably larger couplings than the calculations within FLL for the same value of $U_d$. Besides, $J_{\mathrm{ic1}}$ turns out to be AF in AMF, but FM in FLL. This conspicuous difference between different flavors

of DFT $+\,U$ necessitates an additional examination of this problem by an independent technique.

To this end, we resort to the HSE06 hybrid functional that is free from the DC problem. Here, the DFT exchange is mixed with a fraction of exact (Hartree-Fock) exchange.[34] The HSE06-based exchange integrals (Table IV) are very similar to those obtained using DFT $+\,U$ FLL with $U_d = 3.0$ eV. To check the stability of the HSE06 results, we varied the parameter $\beta$, which reflects the admixture of the exact exchange to the standard DFT exchange ($\beta = 0.25$ in the original definition of HSE06). As follows from the resulting values (Table IV), the increase in $\beta$ from 0.2 to 0.3 is accompanied by the $\sim$25% reduction in the exchange couplings, while the $J_1'/J_1$ ratio is essentially unchanged. Therefore, the effects of increasing $\beta$ in HSE06 and increasing $U_d$ in DFT $+\,U$ are somewhat similar, despite the disparate physical meaning of the $U_d$ and $\beta$ parameters.

On a qualitative level, DFT $+\,U$ FLL, hybrid functionals, and model approach concur with each other on the nature of magnetic couplings in Cr$_2$[BP$_3$O$_{12}$]. By contrast, DFT $+\,U$ AMF predicts the different sign of $J_{\mathrm{ic1}}$, which would render the spin lattice weakly frustrated. However, this scenario looks very unlikely because the independent model analysis (Sec. IV A) yields FM $J_{\mathrm{ic1}}$. Additionally, DFT $+\,U$ AMF systematically overestimates the absolute values of $J_1$ and $J_1'$ (see experimental values in Sec. V) and should probably be discouraged in the case of Cr$_2$[BP$_3$O$_{12}$].[35]

Apart from the overall energy scale of $J_1$ and $J_1'$ that is dependent on $U_d$ or $\beta$ (Table IV), different flavors of DFT $+\,U$, as well as HSE06, predict different $J_1'/J_1$ ratios. Our computational results yield $J_1'/J_1 = 0.39$–0.94, so that $J_1'$ is smaller than $J_1$ but certainly large enough to ensure the quasi-1D nature of the spin lattice. Unfortunately, the more precise evaluation of the $J_1'/J_1$ ratio lies beyond the capabilities of present-day DFT-based techniques and should be addressed by numerical simulations of the spin model and subsequent fitting to the experimental data (see Sec. V).

Finally, we take into account the spin-orbit (SO) coupling and quantify the single-ion anisotropy $D$ using the DFT $+\,U +$ SO calculations within the FLL in VASP. To this end, we calculate total energies (Fig. 1, bottom left) of the AF GS with the magnetic moments aligned parallel and perpendicular to the hexagonal axis ($c$ axis). For $U_d = 3$ eV, the energy difference of 1.3 K slightly favors the in-plane spin arrangement. This result implies a very weak single-ion anisotropy. However, the direction of the magnetic moment should be determined experimentally because the energy difference of 1 K is on the verge of the accuracy of DFT.

In summary, our band structure calculations arrive at a scenario of Heisenberg spin chains with two alternating nearest-neighbor AF interactions $J_1$ and $J_1'$. The magnetic chains are weakly coupled in a nonfrustrated manner by the FM $J_{\mathrm{ic1}}$ and the AF $J_{\mathrm{ic2}}$. While both interchain couplings are apparently weak (below 2 K in terms of the absolute value), the energy scale of the intrachain couplings, as well as the precise alternation ratio, are rather sensitive to details of the computational procedure and require further refinement applying simulation techniques to fit the experimental data.

TABLE V. Results of QMC simulations and fitting to the experimental magnetic susceptibility. $J_1$ and $g$ are obtained from the fits to $\chi(T)$. $T_N/J_1$ is obtained from simulations of spin stiffness (see text). $S_\infty$ is evaluated using Eq. (6). $T_N$ and $m$ are scaled using $J_1$ and $g$ from columns 2 and 3.

| $J_1'/J_1$ | $J_1$ (K) | $g$ | $T_N/J_1$ | $T_N$ (K) | $S_\infty$ | $m(\mu_B)$ |
|---|---|---|---|---|---|---|
| 0.4 | 51.84 | 2.006 | 0.584 | 30.27 | 1.128 | 2.22 |
| 0.5 | 49.51 | 2.002 | 0.642 | 31.79 | 1.151 | 2.27 |
| 0.6 | 47.10 | 1.996 | 0.689 | 32.45 | 1.164 | 2.29 |
| 0.7 | 44.78 | 1.993 | 0.726 | 32.51 | 1.169 | 2.30 |
| 0.8 | 42.58 | 1.992 | 0.755 | 32.15 | 1.165 | 2.29 |

## V. QMC SIMULATIONS AND COMPARISON WITH THE EXPERIMENTS

To refine the parameters of the microscopic magnetic model, we simulate the temperature dependence of the reduced magnetic susceptibility $\chi^*$ for various ratios of $J_1'/J_1$, while keeping the interchain couplings constant $J_{ic2} = -J_{ic1} = 0.02J_1$ (see Table IV), and subsequently fit the simulated QMC curves to the experiment using the expression

$$\chi(T) = \frac{N_A g^2 \mu_B^2}{k_B J_1} \cdot \chi^*\left(\frac{T}{k_B J_1}\right) + \chi_0. \tag{5}$$

Here, the fitted parameters are $J_1$, the Landé factor $g$, and the temperature-independent contribution $\chi_0$.[36] The results are presented in Table V (columns 2 and 3). A general trend is the decrease in $J_1$ upon the increase in $J_1'/J_1$, so that the sum of the leading couplings $J_1 + J_1'$ remains nearly constant ($74.5 \pm 2.0$ K); see also Eq. (4). Still, smaller values of $J_1'/J_1$ yield better agreement with the experimental curve, especially around the maximum in $\chi(T)$.

In general, additional restrictions for the model parameters can be set by the fitted values of $g$. However, $g$ is marginally dependent on $J_1'/J_1$ and shows good agreement with the ESR value of 1.968 in the whole range studied. Therefore, simulation of further measurable quantities is needed to refine the model parameters.

First, we address the magnetic ordering temperature. To this end, we calculate the spin stiffness $\rho$ as a function of temperature for finite lattices with up to $N = L_x \times L_y \times L_z = 13\,824$ spins. At the magnetic ordering transition temperature, the products $\rho_i L_i (i = x,y,z)$ are independent of $L_i$. Thus, $T_N$ is the temperature at which the $\rho L(T)$ curves of the different finite lattices cross. The difference between the simulated values of $T_N$ and its experimental value of 28 K is below 10% for the whole range of $J_1'/J_1$ (see columns 4 and 5 of Table V). Similar to the fits of $\chi(T)$, lower values of $J_1'/J_1$ yield slightly better agreement with the experimental $T_N = 28$ K.

Another measured quantity, which can be used for comparisons between theory and experiment, is the ordered magnetic moment $m$. In the classical $S = 3/2$ Heisenberg model, the ordered magnetic moment $m = g\mu_B S$ amounts to $3\mu_B$, but the experimentally observed moment in $Cr_2[BP_3O_{12}]$ is substantially smaller ($2.5\mu_B$; see Sec. III B). We estimate the reduction in $m$ due to quantum fluctuations. To this end, we simulate the magnetic structure factors $\mathbb{S}$ for finite lattices containing up to 2048 spins.

For the propagation vector **k** of the magnetically ordered GS, the ordered magnetic moment $m$ is evaluated using the finite-size scaling procedure:

$$\frac{3\mathbb{S}(\mathbf{k})}{N} = S_\infty(\mathbf{k})^2 + \frac{\sigma_1}{\sqrt{N}} + \frac{\sigma_2}{N}, \tag{6a}$$

$$m = g\mu_B S_\infty(\mathbf{k}), \tag{6b}$$

where the fitting parameters are $S_\infty(\mathbf{k})$ as well as the expansion coefficients $\sigma_1$ and $\sigma_2$, while $g = 1.968$ is adopted from the ESR.[38] In this way, we arrive at the values that underestimate the experimental result by $\simeq 0.2\mu_B$ (last column of Table V). Since this offset is nearly independent of $J_1'/J_1$, the interchain couplings might be the origin of this discrepancy. Indeed, increasing the interchain couplings by a factor of two ($J_{ic2} = -J_{ic1} = 0.04J_1$) yields $m = 2.49\mu_B$, in excellent agreement with the experiment. However, larger interchain couplings substantially increase the Néel temperature and worsen the agreement between the simulated and experimental $\chi(T)$. Since the experimental value of $T_N$ is more precise than $m$, we argue that the parameters $J_{ic2} = -J_{ic1} = 0.02J_1$ are preferable, while the $0.2\mu_B$ deviation between the experimental and simulated values of $m$ is still reasonable. Indeed, the experimental estimate of $m$ relies upon the available magnetic form factors, as well as on the accuracy of the subtraction procedure. Therefore, we cannot exclude a systematic experimental error in $m$ that should be verified by neutron experiments on single crystals.

As follows from Table V, different values of $J_1'/J_1$ yield rather similar $T_N$ and $m$. This surprisingly robust behavior originates from peculiar properties of spin-$\frac{3}{2}$ alternating Heisenberg chains that show low spin gaps in the $0.41 < J_1'/J_1 < 1$ range between the critical points at $J_1'/J_1 = 0.41$ and $J_1'/J_1 = 1$, where the spin gap vanishes (see Sec. VI and Ref. 39). To evaluate the optimal $J_1'/J_1$, we trace the general trends. First, smaller $J_1'/J_1$ ratios yield better agreement with the experimental $T_N$. Second, $m_{Cr}$ is nearly independent of $J_1'/J_1$ for $J_1'/J_1 \geqslant 0.5$. Thus, the parametrization $J_1 : J_1' : J_{ic1} : J_{ic2} \simeq 1 : 0.5 : -0.02 : 0.02$ with $J_1 \simeq 50$ K is the optimal choice, since it conforms to the experimental $\chi(T)$ dependence, accurately reproduces the experimental $T_N$, as well as the $g$ factor, and is in reasonable agreement with the experimental $m$.

## VI. QUANTUM-CLASSICAL CROSSOVER

For a correct application of classical models, it is crucial to know at which point quantum effects become relevant and the classical approximation breaks down. In this respect, the quasi-1D magnetic model of $Cr_2[BP_3O_{12}]$ is a promising candidate. The leading exchange couplings $J_1$ and $J_1'$ form alternating chains, while the interchain couplings are substantially smaller. Besides, $Cr_2[BP_3O_{12}]$ lacks frustration; thus, quantum MC simulations can be performed.

First, we study nearest-neighbor spin correlations using QMC and classical MC simulations. The difference between the two results is directly related to quantum fluctuations: While QMC correctly accounts for the quantum behavior at finite temperatures, the classical MC method captures thermal fluctuations only.
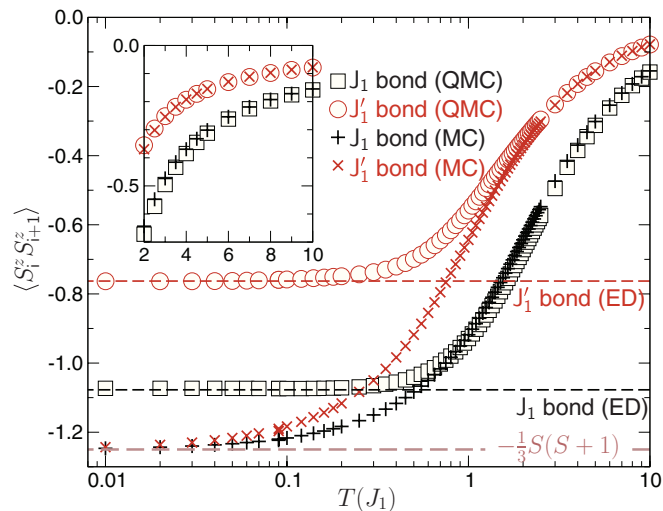
FIG. 6. (Color online) Temperature dependence of the nearest-neighbor diagonal spin correlations $\langle S_i^z S_{i+1}^z \rangle$ in the $S = 3/2$ alternating Heisenberg chain model ($J_1'/J_1 = 0.5$). QMC results are plotted with squares ($J_1$) and circles ($J_1'$); the classical MC results are depicted with pluses ($J_1$) and crosses ($J_1'$). The dashed lines denote the ED results for the quantum model. The $\frac{1}{3}S(S+1)$ line marks the maximal diagonal correlation for $S = 3/2$ spins. (Inset) At high temperatures ($T > 2J_1$), the QMC and MC curves become almost indistinguishable.

In the following, we consider a 1D $J_1 - J_1'$ magnetic model, where the interchain couplings are neglected completely. For $J_1'/J_1 = 0.5$, we simulate the temperature dependence of the diagonal spin correlations $\langle S_i^z S_{i+1}^z \rangle$ and $\langle S_{i+1}^z S_{i+2}^z \rangle$, where $i = 0$ corresponds to the stronger coupling $J_1$, while $i = 1$ corresponds to $J_1'$.

The resulting curves are plotted in Fig. 6. In the high-temperature range (see inset in Fig. 6), the classical and quantum results are practically indistinguishable. At $T \simeq J_1$, the curves start to deviate significantly. The classical MC curves exhibit an asymptotic behavior and join at $T = 0$. This is in line with a complete elimination of thermal fluctuations; thereby, the spin correlations reach their extremal value for $S = 3/2$ spins, which amounts to $-[S(S+1)]/3 = -1.25$.

Although the QMC curves exhibit qualitatively similar behavior at low temperatures, they saturate at substantially higher values of $\langle S_i^z S_{i+1}^z \rangle$. Dissimilar to the classical model, the $i = 0$ ($J_1$) and $i = 1$ ($J_1'$) QMC curves saturate at different values of $\langle S_i^z S_{i+1}^z \rangle$, indicating the onset of dimerization.

In the vicinity of the broad maximum of the magnetic susceptibility ($T^{\max} \simeq 2 J_1$), and even at lower temperatures, the classical MC simulations are in excellent agreement with the quantum model. Therefore, experimental thermodynamic data [e.g., $\chi(T)$ and magnetic specific heat] for $T \gtrsim J_1$ should be well reproduced within the classical approximation. This empirical rule follows earlier experimental and numerical results for uniform spin-$\frac{3}{2}$ chains.[9] It can also be generalized to quasi-2D and 3D systems, owing to further suppression of quantum fluctuations in higher dimensions. However, in 0D systems, such as isolated dimers, quantum effects are expected to play a more substantial role.
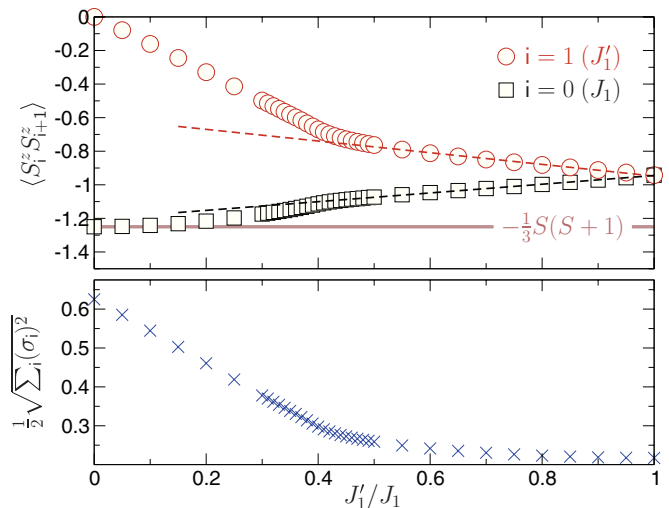


FIG. 7. (Color online) (Top) Nearest-neighbor diagonal spin correlations $\langle S_i^z S_{i+1}^z \rangle$ in the $S = 3/2$ alternating Heisenberg chain model as a function of the alternation ratio $J_1'/J_1$ at $T = 0.03J_1$. Dashed lines are guides for the eye. (Bottom) Root mean square of $\sigma_i \equiv (\langle S_i^z S_{i+1}^z \rangle - \frac{1}{3}S[S+1])$ ($i = 1, 2$), reflecting the discrepancy between the quantum and the classical models.

To explore the evolution of quantum fluctuations by a gradual crossover from 1D to 0D regime, we evaluate the GS diagonal spin correlations for different ratios $J_1'/J_1$. Although QMC simulations are not applicable at $T = 0$, the temperature evolution of spin correlations in Fig. 6 suggests only a marginal change in $\langle S_i^z S_{i+1}^z \rangle$ below $0.03J_1$. Thus, finite-temperature spin correlations simulated at $T = 0.03J_1$ can be regarded as a rather accurate measure of GS ($T = 0$) spin correlations.

Figure 7 (top) shows the resulting $\langle S_i^z S_{i+1}^z \rangle (J_1'/J_1)$ dependencies. In the uniform-chain limit ($J_1'/J_1 = 1$), the correlations for $i = 0$ and 1 coincide. Dimerization gives rise to a quasilinear behavior observed down to $J_1'/J_1 \simeq 0.4$. At this point, both curves exhibit a pronounced kink, and their further evolution is different: The $i = 0$ ($J_1$) curve rapidly drops almost down to the extremal value $\frac{1}{3}S[S+1]$, while the $i = 1$ ($J_1'$) curve exhibits a quasilinear growth up to zero correlation in the $J_1'/J_1 = 0$ limit. This behavior is remarkably different from the classical case, where the constant spin-spin correlation of $-\frac{1}{3}S(S+1)$ is expected.

To sharpen the crossover at $J_1'/J_1 \simeq 0.4$, we consider root mean square deviation for $\sigma_i \equiv (\langle S_i^z S_{i+1}^z \rangle - \frac{1}{3}S(S+1))$ ($i = 1, 2$), which reflects the difference between the quantum and classical models. The resulting dependence is shown in Fig. 7 (bottom). For $0.5 \leqslant J_1'/J_1 \leqslant 1$, only a marginal increase is observed, while at $J_1'/J_1 \simeq 0.4$ the slope changes distinctly. For $J_1'/J_1 < 0.4$, a quasilinear behavior is restored.

The drastic change in the spin-spin correlations around $J_1'/J_1 \simeq 0.4$ indicates the critical point of bond-alternating spin-$\frac{3}{2}$ chains. While such chains generally have gapped GS, they become gapless in the uniform-chain limit ($J_1'/J_1 = 1$) and at the critical point of $J_1'/J_1 \simeq 0.41$, according to density-matrix renormalization group[39] and QMC studies.[40] Qualitatively, the critical point at $J_1'/J_1 \simeq 0.41$ can be understood as the transition between two different valence-bond-solid (VBS)-type GSs.

The VBS state entails singlet pairs formed by individual spin-$\frac{1}{2}$ entities comprising spin-$\frac{3}{2}$ sites of the lattice.[41] Although it is not an exact GS of the Heisenberg Hamiltonian in Eq. (1), the references to relevant VBS states are instrumental in understanding peculiarities of the magnetic behavior. The spin-$\frac{3}{2}$ chain can form two VBS states, the (3,0) state having three singlet pairs on one bond and no pairs on the contiguous bonds, or the (2,1) state having two singlet pairs on one bond and one singlet pair on each of the neighboring bonds. At low $J_1'/J_1$, alternating spin-$\frac{3}{2}$ chains are close to the (3,0) regime, as shown by the drastic difference between the spin-spin correlations for $J_1$ and $J_1'$. At $J_1'/J_1 > 0.41$, the system resembles the (2,1) VBS[40] and eventually develops the GS of a uniform spin-$\frac{3}{2}$ chain with equal correlations on the $J_1$ and $J_1'$ bonds (Fig. 7). Note that the low-temperature physics of alternating spin-$\frac{3}{2}$ chains is essentially governed by quantum effects and cannot be reproduced in the classical approximation.

## VII. DISCUSSION AND SUMMARY

The formation of alternating spin chains contrasts with the presence of isolated $Cr_2O_9$ dimers in the crystal structure of $Cr_2[BP_3O_{12}]$. However, such differences between the structure and the ensuing spin lattice are not unusual, especially for phosphates, vanadates, and other compounds with complex anions that are capable of mediating the superexchange. For example, a large superexchange coupling via the $PO_4$ tetrahedra between the structural dimers is a salient feature of the spin-$\frac{1}{2}$ alternating-chain magnet $(VO)_2[P_2O_7]$ (Ref. 26). In spin-$\frac{1}{2}$ $V^{4+}$ and $Cu^{2+}$ compounds, interdimer couplings often exceed the intradimer exchange, whereas the latter is small or even negligible, as in $Cu_2[P_2O_7]$ (Ref. 28) or $VO[HPO_4] \cdot \frac{1}{2}H_2O$ (Ref. 42).

The $Cr_2[BP_3O_{12}]$ case is different, though, because the intradimer coupling $J_1$ exceeds the interdimer coupling $J_1'$. The reason behind the sizable intradimer coupling is the strong direct exchange that was previously observed in $LiCrO_2$.[32] While the Cr-O-Cr angles amount to 87.8° and impede the AF superexchange, the direct overlap of Cr $d$ orbitals is strong enough to facilitate the sizable AF $J_1$. This mechanism is not operative in typical spin-$\frac{1}{2}$ systems with structural dimers, because $V^{4+}$ cations form $VO_5$ square pyramids and remain on opposite sides of the basal plane of such pyramids, thus featuring only a weak direct overlap of the magnetic $d_{xy}$ orbitals. In the case of $Cu^{2+}$, the magnetic orbital has the $d_{x^2-y^2}$ symmetry, unfavorable for the direct overlap.

It is also instructive to compare different interdimer couplings in $Cr_2[BP_3O_{12}]$. Similar to other transition-metal phosphates,[27,28] the Cr-based WFs show sizable contributions of Cr $3d$ and O $2p$ states only (Fig. 5). Phosphorous states weakly contribute to the magnetic orbitals and play a minor role in the superexchange running via the Cr-O$\cdots$O-Cr pathways. The efficiency of these pathways intimately depends on details of the crystal structure.

Remarkably, $Cr_2[BP_3O_{12}]$ not only entails the spin lattice of alternating chains, but also features the alternation ratio of $J_1'/J_1 \simeq 0.5$, which is close to the critical point with the gapless ground state at $J_1'/J_1 \simeq 0.41$. The proximity to this

critical point is one of the reasons behind the long-range AF ordering and the sizable Néel temperature in $Cr_2[BP_3O_{12}]$. Spin-$\frac{1}{2}$ systems with the larger $J_1'/J_1 \simeq 0.6$ (i.e., weaker dimerization) and comparable interchain couplings[43] still have the spin-gap ground state, as in $Pb_2[V_3O_9]$ (Ref. 44) and $Ag(VO)[AsO_4]$ (Ref. 45). The large number of interchain couplings per magnetic site (the coordination number amounts to six and three for $J_{ic1}$ and $J_{ic2}$, respectively), as found in $Cr_2[BP_3O_{12}]$, may also reduce quantum fluctuations. By contrast, an isolated alternating $S=3/2$ chain with $J_1'/J_1 \simeq 0.5$ would feature an excitation gap of $\sim 0.25\,J_1$ with no long-range order.[40]

While the critical point at $J_1'/J_1 \simeq 0.41$ has been widely studied theoretically,[39,40] experimental probes of this regime and even experimental examples of spin-$\frac{3}{2}$ alternating chains have not been reported. Therefore, $Cr_2[BP_3O_{12}]$ may be interesting as an experimentally available spin-$\frac{3}{2}$ alternating-chain system in the vicinity of this critical point. Although $Cr_2[BP_3O_{12}]$ is not perfectly 1D and features the long-range AF order owing to nonzero interchain couplings, an experimental study of spin-spin correlations with, e.g., inelastic neutron scattering, could be instructive. Moreover, the application of external pressure might change the $J_1'/J_1$ ratio, thus giving access to the peculiar evolution of spin-spin correlations across the critical point (Fig. 7). Detailed studies of the isostructural phase $Fe_2[BP_3O_{12}]$ (Ref. 23) may be instructive as well, because this compound should feature a similar spin lattice in the more classical regime of spin-$\frac{5}{2}$.

In summary, we extensively characterized the magnetic behavior of $Cr_2[BP_3O_{12}]$ using magnetic susceptibility, neutron diffraction, and ESR measurements. The long-range AF order established below $T_N = 28$ K is described with the propagation vector $\mathbf{k} = 0$, whereby the spins on nearest-neighbor Cr atoms within the $ab$ plane, as well as along the $c$-axis direction, are antiparallel. On the microscopic level, $Cr_2[BP_3O_{12}]$ features $S = 3/2$ Heisenberg chains with an alternation of the nearest-neighbor couplings $J_1$ and $J_1'$. The ratio $J_1'/J_1 \simeq 0.5$ renders $Cr_2[BP_3O_{12}]$ as an interesting model system lying close to the critical point at $J_1'/J_1 \simeq 0.41$, where the spin-$\frac{3}{2}$ alternating chain has the gapless ground state. The chains are coupled by two nonequivalent interchain exchanges: the FM $J_{ic1}$ and the AF $J_{ic2}$, both of the order of 1 K–2 K. The microscopic model is in excellent agreement with the experimental magnetic structure (see Fig. 1): The nearest-neighbor spins within a chain are antiparallel, in accord with the AF nature of $J_1$ and $J_1'$. Moreover, even the interchain coupling regime is compatible with FM $J_{ic1}$ and AF $J_{ic2}$; thus, $Cr_2[BP_3O_{12}]$ lacks any appreciable frustration effects.

*janson@cpfs.mpg.de

†altsirlin@gmail.com

‡rosner@cpfs.mpg.de

[1] H. Bethe, Z. Phys. A **71**, 205 (1931); C. K. Majumdar and D. K. Ghosh, J. Math. Phys. **10**, 1388 (1969); **10**, 1399 (1969).

[2] B. S. Shastry and B. Sutherland, Physica B + C (Amsterdam) **108**, 1069 (1981).

[3] R. Dingle, M. E. Lines, and S. L. Holt, Phys. Rev. **187**, 643 (1969); M. T. Hutchings, G. Shirane, R. J. Birgeneau, and S. L. Holt, Phys. Rev. B **5**, 1999 (1972).

[4] W. J. M. de Jonge, J. P. A. M. Hijmans, F. Boersma, J. C. Schouten, and K. Kopinga, Phys. Rev. B **17**, 2922 (1978).

[5] S. Itoh, H. Tanaka, and T. Otomo, J. Phys. Soc. Jpn. **66**, 455 (1997); S. Itoh, H. Tanaka, and M. J. Bull, ibid. **71**, 1148 (2002).

[6] For example, P. Chandra and B. Doucot, Phys. Rev. B **38**, 9335 (1988); E. Dagotto and A. Moreo, ibid. **39**, 4744 (1989).

[7] For example, I. Rousochatzakis, A. M. Läuchli, and R. Moessner, Phys. Rev. B **85**, 104415 (2012).

[8] F. D. M. Haldane, Phys. Rev. Lett. **50**, 1153 (1983).

[9] S. Itoh, Y. Endoh, K. Kakurai, and H. Tanaka, Phys. Rev. Lett. **74**, 2375 (1995); S. Itoh, Y. Endoh, K. Kakurai, H. Tanaka, S. M. Bennington, T. G. Perring, K. Ohoyama, M. J. Harris, K. Nakajima, and C. D. Frost, Phys. Rev. B **59**, 14406 (1999).

[10] C. Payen, H. Mutka, J. Soubeyroux, P. Molinié, and P. Colombet, J. Magn. Magn. Mater. **104-107**, 797 (1992); H. Mutka, C. Payen, and P. Molinie, Europhys. Lett. **21**, 623 (1993).

[11] M. P. Pechini, US patent 3.330.397 (1967) .

[12] J.-X. Mi, J.-T. Zhao, S.-Y. Mao, Y.-X. Huang, H. Engelhardt, and R. Kniep, Z. Kristallogr. New Cryst. Struct. **215**, 201 (2000).

[13] The $^{11}$B-containing compound (H$_3^{11}$BO$_3$) has been used to prepare samples for neutron powder diffraction.

[14] A. Larson and R. von Dreele, Los Alamos National Laboratory Report LAUR 86-748, 1994 .

[15] J. Rodríguez-Carvajal, Physica B **192**, 55 (1993).

[16] K. Koepernik and H. Eschrig, Phys. Rev. B **59**, 1743 (1999).

[17] G. Kresse and J. Furthmüller, Phys. Rev. B **54**, 11169 (1996); Comput. Mater. Sci. **6**, 15 (1996).

[18] J. P. Perdew and Y. Wang, Phys. Rev. B **45**, 13244 (1992).

[19] J. P. Perdew, K. Burke, and M. Ernzerhof, Phys. Rev. Lett. **77**, 3865 (1996).

[20] J. Heyd, G. E. Scuseria, and M. Ernzerhof, J. Chem. Phys. **118**, 8207 (2003); J. Heyd and G. E. Scuseria, ibid. **121**, 1187 (2004).

[21] Large computational demands incurred by the hybrid functionals lead to severe restrictions on the number of $k$ points. Nevertheless, the results obtained on a sparse $k$ mesh are sufficiently accurate and well converged, owing to the insulating nature of Cr$_2$[BP$_3$O$_{12}$].

[22] A. Albuquerque et al., J. Magn. Magn. Mater. **310**, 1187 (2007).

[23] W.-L. Zhang, C.-S. Lin, L. Geng, Y.-Y. Li, H. Zhang, Z.-Z. He, and W.-D. Cheng, J. Solid State Chem. **183**, 1108 (2010); F. F. Li, H. J. Zhang, and L. N. Zhang, Acta Crystallogr. Sect. E **66**, i63 (2010).

[24] M. Campostrini, M. Hasenbusch, A. Pelissetto, P. Rossi, and E. Vicari, Phys. Rev. B **65**, 144520 (2002); A. Pelissetto and E. Vicari, Phys. Rep. **368**, 549 (2002).

[25] See Supplemental Material at http://link.aps.org/supplemental/10.1103/PhysRevB.87.064417 for the crystal structure refinement, ESR data, the low-temperature magnetization data, as well as LSDA and GGA density of states for the ferromagnetic solution.

[26] A. W. Garrett, S. E. Nagler, D. A. Tennant, B. C. Sales, and T. Barnes, Phys. Rev. Lett. **79**, 745 (1997).

[27] A. A. Tsirlin, R. Nath, C. Geibel, and H. Rosner, Phys. Rev. B **77**, 104436 (2008).

[28] O. Janson, A. A. Tsirlin, J. Sichelschmidt, Y. Skourski, F. Weickert, and H. Rosner, Phys. Rev. B **83**, 094435 (2011); S. Lebernegg, A. A. Tsirlin, O. Janson, R. Nath, J. Sichelschmidt, Y. Skourski, G. Amthauer, and H. Rosner, ibid. **84**, 174436 (2011).

[29] Here, we do not adapt the local coordinate frame to the global symmetry of the crystal structure, and direct the local $z$ axis along one of the Cr-O bonds (see also Fig. 5). Therefore, the resulting $d$ states do not show the weak splitting in the $t_{2g}$ subspace, as expected for trigonally distorted octahedron. This simplification does not affect any of our results, because Cr$^{3+}$ shows the robust high-spin state with the half-filled $t_{2g}$ levels, whereas fine structure of these levels has a minor effect on the magnetism.

[30] D. C. Johnston, R. K. Kremer, M. Troyer, X. Wang, A. Klümper, S. L. Bud'ko, A. F. Panchula, and P. C. Canfield, Phys. Rev. B **61**, 9558 (2000).

[31] M. T. Czyżyk and G. A. Sawatzky, Phys. Rev. B **49**, 14211 (1994).

[32] I. I. Mazin, Phys. Rev. B **75**, 094407 (2007).

[33] C. J. Fennie and K. M. Rabe, Phys. Rev. Lett. **96**, 205505 (2006).

[34] C. Franchini, R. Podloucky, J. Paier, M. Marsman, and G. Kresse, Phys. Rev. B **75**, 195128 (2007); F. Iori, M. Gatti, and A. Rubio, ibid. **85**, 115129 (2012).

[35] It is widely believed that for insulators only the FLL DC correction is appropriate. By the same token, thorough studies of magnetic couplings in Cu and V oxides show that AMF may provide comparable or even better results than FLL, although in a rather unsystematic fashion: See, e.g., A. A. Tsirlin, O. Janson, and H. Rosner, Phys. Rev. B **82**, 144416 (2010); **84**, 144429 (2011).

[36] For the fitting, we used the experimental data above $T_N = 28$ K, since a 1D model cannot account for the AF ordering (Ref. 37).

[37] N. D. Mermin and H. Wagner, Phys. Rev. Lett. **17**, 1133 (1966).

[38] Unfortunately, the quasi-1D character of the magnetic model requires $L_z \gg L_x \simeq L_y$ for an $N$-site lattice ($N = L_x \times L_y \times L_z$). This leads to a small number of computationally feasible lattices, impeding an accurate estimation of the magnetic moment. To check the results for consistency, we repeated the fitting using a simplified scaling $\sigma_2 = 0$. As expected, the $\sigma_1$ values are substantially renormalized. Yet, both approaches yield marginally different values of $S_\infty$ (∼1% difference).

[39] M. Yajima and M. Takahashi, J. Phys. Soc. Jpn. **65**, 39 (1996).

[40] S. Yamamoto, Phys. Rev. B **55**, 3603 (1997).

[41] I. Affleck, T. Kennedy, E. H. Lieb, and H. Tasaki, Phys. Rev. Lett. **59**, 799 (1987); Commun. Math. Phys. **115**, 477 (1988).

[42] D. A. Tennant, S. E. Nagler, A. W. Garrett, T. Barnes, and C. C. Torardi, Phys. Rev. Lett. **78**, 4998 (1997).

[43] The interchain couplings should be considered irrespective of their sign and together with the relevant coordination numbers. In Cr$_2$[BP$_3$O$_{12}$], the effective interchain coupling is $J_{eff} = 3J_{ic2} + 6|J_{ic1}| = 0.18J_1$, i.e., $J_{ic}/J_1 = 0.09$ for the typical coordination number of 2 (as, e.g., in Pb$_2$V$_3$O$_9$).

[44] A. A. Tsirlin and H. Rosner, Phys. Rev. B **83**, 064415 (2011).

[45] A. A. Tsirlin, R. Nath, J. Sichelschmidt, Y. Skourski, C. Geibel, and H. Rosner, Phys. Rev. B **83**, 144412 (2011).